Total Pressure Loss in Vortical Solutions of the Conical Euler Equations

Kenneth G. Powell,* Earll M. Murman,† Eric S. Perez,‡ and Judson R. Baron†
Massachusetts Institute of Technology, Cambridge, Massachusetts

A technique for the solution of the conically self-similar form of the Euler equations is described. Solutions for the flow past a flat-plate delta wing at angle of attack ($M_\infty = 1.5, \Lambda = 70$ deg, $\alpha = 10$ deg) are presented. These solutions show strong leading-edge vortices with large total pressure losses in the cores. A study of the effects of various computational parameters on the total pressure loss is made. An explanation for the cause of the total pressure loss is presented. It is shown to be consistent with the results for both a quasi-one-dimensional model problem and the conically self-similar flow past the flat-plate delta wing.

Introduction

THE flow past a delta wing at angle of attack can exhibit a variety of structures, depending on the geometry of the wing, angle of attack, and freestream Mach number.[1] The structure of the flow past a highly swept wing, even at low Mach numbers and angles of attack, is characterized by strong primary vortices on the leeward side. These vortices dramatically affect the aerodynamics of the wing and, thus, their prediction is of great importance to designers. Shock waves may be generated by the vortical flow. Secondary vortices may be generated by either boundary-layer separation under the primary vortex or embedded cross-flow shocks.

Flows with leading-edge vortices may be modeled by the potential equation (with fitted vortex sheets),[2] Euler equations,[3-5] or Navier-Stokes equations.[6-8] Each of these models has advantages and disadvantages.[9] The potential equation requires the least computational resources to solve, but is limited at present to incompressible potential flow with fitted vortex sheets. The Euler equations require greater computational resources and, although they model distributed vorticity and shocks, they do not model the viscous effects. The Navier-Stokes equations model the viscous effects and permit solutions with distributed vorticity and shocks, but are the most expensive computationally. In this paper, the Euler equation model is adopted.

The first disadvantage of the Euler equations as a model—that they require large amounts of computer storage and time to solve—is becoming less crucial as computer capacity increases and the algorithms for solving such equations evolve. However, three-dimensional solutions with good resolution still require vast amounts of storage and time.[10,11] In the case of the flow past a delta wing, significant savings may be made by restricting the class of problems to be solved to conically self-similar wings in steady supersonic freestreams.[12] With this restriction, only two independent spatial variables are necessary to solve the three-dimensional inviscid equations.

The second disadvantage of the Euler equations as a model—that they do not model viscous effects—is less crucial for some problems than for others. For a sharp-edge geometry, the separation point is fixed at the leading edge, independent of the Reynolds number. The dissipation introduced by the spatial discretization of the Euler equations should mimic the physical viscosity and cause separation. Just as the separation point is insensitive to the real viscosity, it should also be insensitive to the artificial viscosity. Computational experience shows this to be the case. Therefore, the Euler equation model contains a means for inducing separation and creating a primary vortex. Although secondary vortices brought about by viscous effects on the leeward side of the wing will not be modeled, their effects on the primary vortices are small, as has been shown by comparison of Euler and Navier-Stokes solutions.[6]

The Euler equation solutions presented by the authors were obtained by a finite-volume multistage scheme. The scheme will be outlined here, but is more fully documented in Refs. 13 and 14. All of the solutions exhibit large total pressure losses at the cores of the leading-edge vortices, four orders of magnitude greater than the total pressure loss across the bow shock. Total pressure losses of similar size and distribution are evident in solutions generated by other researchers as well, in both Euler solutions[10] and Navier-Stokes solutions.[6,7]

This paper addresses the question of the source of these total pressure losses. A study of the effects of various computational parameters on the magnitude of the total pressure loss is made. The evolution of the total pressure loss is studied by plotting the distribution of total pressure loss at different points in the iteration history. A model for the total pressure loss is presented and confirmed by the results of a quasi-one-dimensional model problem and those of the leading-edge vortex solutions.

Governing Equations

The three-dimensional unsteady Euler equations in conservation form are

$$\frac{\partial}{\partial t}\begin{bmatrix}\rho\\ \rho u\\ \rho v\\ \rho w\\ \rho E\end{bmatrix}+\frac{\partial}{\partial x}\begin{bmatrix}\rho u\\ \rho u^2+p\\ \rho uv\\ \rho uw\\ \rho uh_0\end{bmatrix}+\frac{\partial}{\partial y}\begin{bmatrix}\rho v\\ \rho uv\\ \rho v^2+p\\ \rho vw\\ \rho vh_0\end{bmatrix}+\frac{\partial}{\partial z}\begin{bmatrix}\rho w\\ \rho uw\\ \rho vw\\ \rho w^2+p\\ \rho wh_0\end{bmatrix}=0 \tag{1}$$

Presented as Paper 85-1701 at the AIAA 18th Fluid Dynamics, Plasmadynamics and Lasers Conference, Cincinnati, OH, July 16–18, 1985; received Aug. 26, 1985; revision received July 11, 1986.

*Research Assistant. Member AIAA.
†Professor. Associate Fellow AIAA.
‡Research Assistant.

The equation of state

$$\frac{p}{\rho} = (\gamma - 1)\left[E - \frac{u^2 + v^2 + w^2}{2}\right] \tag{2}$$

and the supplementary relation

$$h_0 = E + p/\rho \tag{3}$$

close the set of equations. Introducing the conical variables,

$$\eta = y/x, \qquad \xi = z/x, \qquad r = \sqrt{x^2 + y^2 + z^2} \tag{4}$$

and assuming conical self-similarity, the Euler equations become

$$\frac{r}{\sqrt{1+\eta^2+\xi^2}}\frac{\partial}{\partial t}\begin{bmatrix}\rho\\ \rho u\\ \rho v\\ \rho w\\ \rho E\end{bmatrix} + \frac{\partial}{\partial \eta}\begin{bmatrix}\rho(v-\eta u)\\ \rho u(v-\eta u)-\eta p\\ \rho v(v-\eta u)+p\\ \rho w(v-\eta u)\\ \rho h_0(v-\eta u)\end{bmatrix} + \frac{\partial}{\partial \xi}\begin{bmatrix}\rho(w-\xi u)\\ \rho u(w-\xi u)-\xi p\\ \rho v(w-\xi u)\\ \rho w(w-\xi u)+p\\ \rho h_0(w-\xi u)\end{bmatrix} + 2\begin{bmatrix}\rho u\\ \rho u^2+p\\ \rho uw\\ \rho uw\\ \rho u h_0\end{bmatrix} = 0 \tag{5}$$

In the above, the unsteady terms have been retained for the iterative procedure used to reach the steady, conically self-similar solution. Another form of the equations, outlined more fully by Murman et al.,[12] has also been used. It includes metric terms inside the flux vectors. The two forms are mathematically equivalent and a comparison of numerical solutions shows that either may be used.

Solution Procedure

The basic solution scheme is a finite-volume spatial discretization with a multistage integration in time, as proposed by Jameson et al.[15] A set of partial differential equations of the form

$$\frac{\partial}{\partial t}\boldsymbol{U} + \frac{\partial}{\partial \eta}\boldsymbol{F} + \frac{\partial}{\partial \xi}\boldsymbol{G} + \boldsymbol{H} = 0 \tag{6}$$

is discretized as

$$\frac{\mathrm{d}\boldsymbol{U}_{ij}}{\mathrm{d}t}A_{ij} + \sum_{l=1}^{4}\left[\boldsymbol{F}_l n_{\xi_l} + \boldsymbol{G}_l n_{\eta_l}\right] + \boldsymbol{H}_{ij}A_{ij} = 0 \tag{7}$$

This scheme requires added second- and fourth-order damping to capture shocks and yield smooth solutions. The damping formulation adopted follows Rizzi and Eriksson.[16] The second-order damping is pressure weighted and of the form

$$\boldsymbol{D}_2(\boldsymbol{U}) = \nu_2\left[\delta_i\left(\frac{\delta_i^2 p}{\max|\delta_i^2 p|}\delta_i \boldsymbol{U}\right) + \delta_j\left(\frac{\delta_j^2 p}{\max|\delta_j^2 p|}\delta_j \boldsymbol{U}\right)\right] \tag{8}$$

where δ_i and δ_j are undivided central difference operators defined by

$$\delta_i(\boldsymbol{U}_{i,j}) = \boldsymbol{U}_{i+\frac{1}{2},j} - \boldsymbol{U}_{i-\frac{1}{2},j} \qquad \delta_j(\boldsymbol{U}_{i,j}) = \boldsymbol{U}_{i,j+\frac{1}{2}} - \boldsymbol{U}_{i,j-\frac{1}{2}} \tag{9}$$

The fourth-order damping is unweighted and of the form

$$\boldsymbol{D}_4(\boldsymbol{U}) = \nu_4\left[\delta_i^4 \boldsymbol{U} + \delta_j^4 \boldsymbol{U}\right] \tag{10}$$

It is not turned off in the vicinity of shocks.

The body boundary condition is a pressure extrapolation of the form

$$p_{j_{\text{body}}} = p_{j=1} \tag{11}$$

This is consistent, since the radius of curvature is infinite on each side of the plate and the $j = \text{const}$ grid lines are normal to the plate.

The far-field boundary condition is enforced by a characteristic-based scheme. The bow shock is interior to the computational domain and is captured. This is preferable to fitting the bow shock, since the bow shocks for the cases in this paper are very weak. The bow-shock capturing method is less expensive computationally and provides a better spectral radius than the bow-shock fitting procedure. It should be noted that the bow shocks in the cases in this paper are weak enough that the total pressure losses across them are at least four orders of magnitude smaller than those in the vortex cores.

The grid is generated by a conformal mapping. The (η, ξ) plane is transformed to a complex ζ plane in which the flat plate becomes a circle. This is achieved by a Joukowski transformation of the form

$$\xi + i\eta = \zeta + \frac{\tan^2[(\pi/2) - \Lambda]}{2\zeta} \tag{12}$$

Grid points are generated along rays in the ζ plane by the formulas

$$r_i = -\log\left[1 - \left(\frac{1 - e^{-\beta}}{\beta}\right)\left(\frac{i-1}{i_{\max}-1}\right)\right] \tag{13}$$

$$\zeta_{ij} = \zeta_{\text{body}_j} + \left[\zeta_{\text{shock}_j} - \zeta_{\text{body}_j}\right] r_i \tag{14}$$

in which β is a stretching parameter. This radial distribution, proposed by Marconi,[17] is linear near the body in the limit of small β.

Computational Results

Figures 1–6 present the solution of the delta wing problem, with the baseline values for all parameters listed in Table 1.

Figure 1 is the grid for this case. The Joukowski transformation used to generate the grid ensures that the grid lines are normal to the body and that the tip region is well resolved. Figures 2 and 3 show the pressure coefficient on the body and in the field. The low-pressure region under the vortex and the expansion around the leading edge are the dominant features, although it is also interesting to note the small constant-pressure region on the leeward side near the leading edge. The cross-flow Mach number distribution in the field is presented in Fig. 4. There are four cross-flow stagnation points on the body: one each at the windward point of symmetry, at the leeward point of symmetry, on the windward side near the leading edge, and on the leeward side not far from the point of symmetry. There is also a cross-flow stagnation point in the core of the vortex. At these points the flow is purely radial. The radial Mach number in the field is shown in Fig. 5. Figure 6 illustrates the total pressure loss in the field, normalized by the freestream total pressure outside the bow shock $(1 - P_t/P_{t_\infty})$. The loss across the bow shock is very small (0.003% on the windward side) compared to the losses in the vortex. The vortex is clearly defined, with a sheet (four or five grid cells thick) emanating from the leading edge and rolling into a diffuse vortex core.

Table 1 Baseline values of parameters

Freestream Mach number	$M_\infty = 1.5$
Leading-edge sweep	$\Lambda = 70$ deg
Angle of attack	$\alpha = 10$ deg
Coefficient of second-difference damping	$\nu_2 = 0.05$
Coefficient of fourth-difference damping	$\nu_4 = 0.01$
Grid stretching parameters	$\beta = 2.5$
Number of cells	$i_{max} = j_{max} = 64$

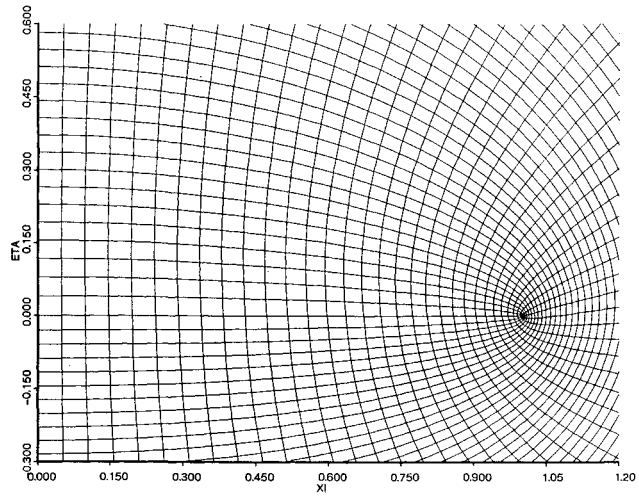

Fig. 1 Grid.

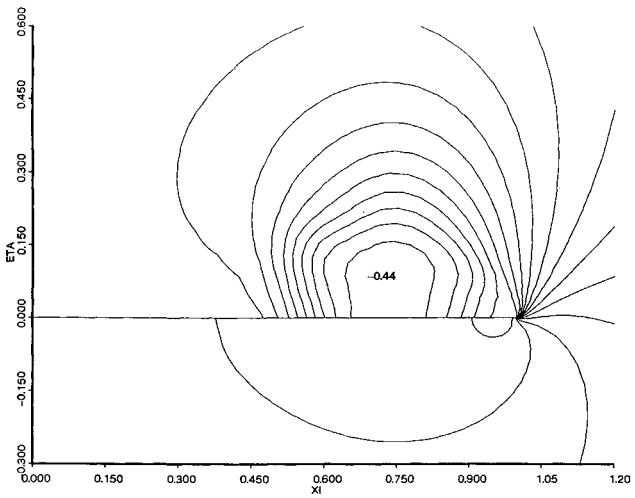

Fig. 2 Pressure coefficient contours (increment = 0.04).

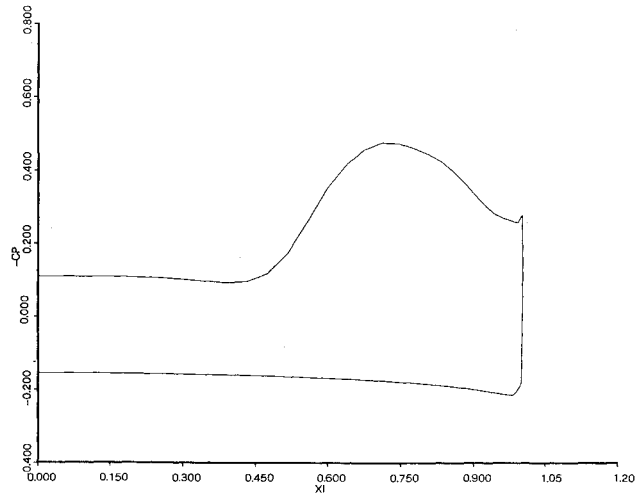

Fig. 3 Pressure coefficient on the wing.

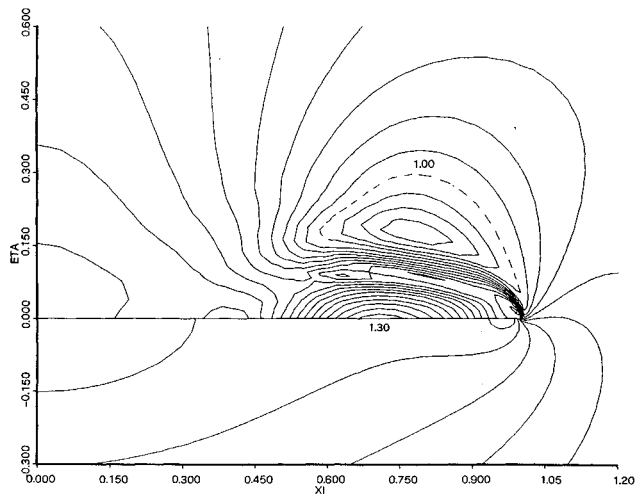

Fig. 4 Cross-flow Mach number contours (increment = 0.10).

Figure 7 shows the evolution of the vortex during the computation. The total pressure loss and the body pressure coefficient are shown at various points in the convergence. The total pressure loss, generated at the tip, is swept toward the leeward symmetry point and rolls up into a smaller version of the final vortex. The losses in the core are higher during the transients than they are in steady state. The pressure coefficient shows the low-pressure region forming almost immediately and then spreading out along the leeward side of the wing.

Figure 8 illustrates the effects (or lack thereof) of changing the artificial viscosity levels by an order of magnitude. There are no appreciable changes in the core total pressure loss. The only change in evidence is in the total pressure loss on the body. Lowering the coefficient of the second-order damping leads to larger negative losses on the body, which seem to be associated with a negative spike at the leading edge. Although the magnitude of the total pressure loss is not appreciably affected by the level of artificial viscosity, the larger viscosity coefficients generate more diffuse vortices.

The effects of changing the grid distribution are presented in Fig. 9. The stretching parameter β is varied and the grids and total pressure loss distributions that result are shown. Figure 10 shows the results of changing the grid refinement. Total pressure losses are shown for 32×32 and 128×128 grids. The vortex is better defined on the higher-resolution meshes, but the magnitude of the losses and the location of the maximum loss are almost the same on all of the grids.

Other published investigations indicate total pressure losses of the order of magnitude reported here and show the same general insensitivity to computational parameters. Solutions by Rizzi[10] of the full three-dimensional Euler equations, with the energy equation replaced by a constant total enthalpy condition, yield a total pressure loss of 60% for this same case. Rizetta and Shang[6] have directly compared Euler with Navier-Stokes solutions on H-type grids for a different wing geometry at $M_\infty = 1.95$. The total pressure loss was 70% and its magnitude was not influenced by the inclusion of the viscous terms.

The results of these numerical experiments may be summarized by the statement that the magnitude of the total pressure loss in the vortex cores is relatively insensitive to every computational parameter, grid topology, and governing

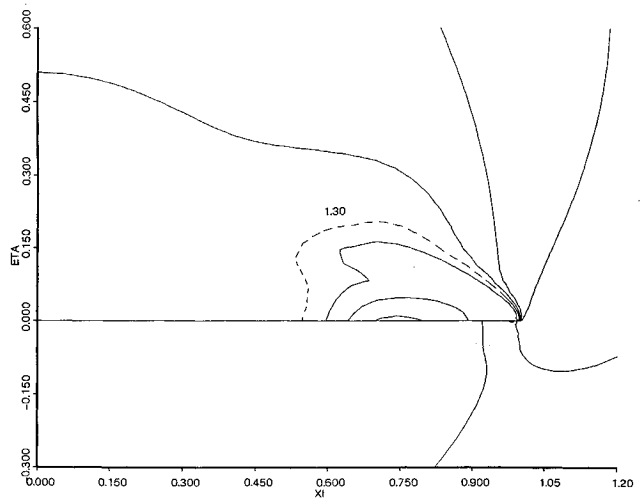

Fig. 5 Radial Mach number contours (increment = 0.10).

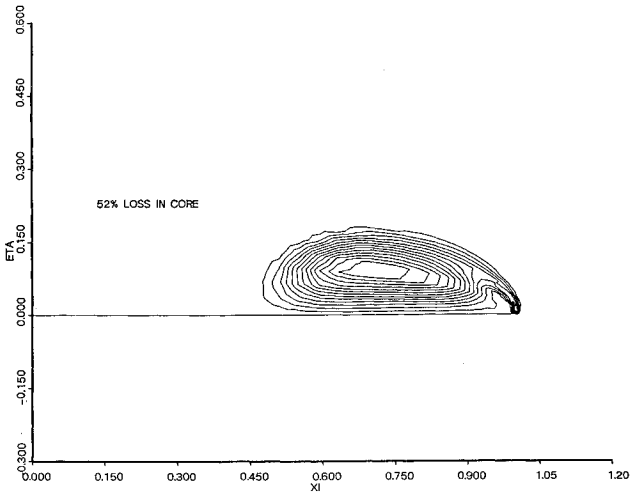

Fig. 6 Total pressure loss contours (increment = 0.04).

equation and boundary condition formulation studied to date. The distribution of the total pressure loss is influenced by the computational parameters, with increased dissipation due to the lack of grid refinement, viscous terms, or added artificial viscosity yielding more diffuse vorticies. The total pressure loss does depend on α, Λ, and M_∞, although these calculations are not reported here. An explanation of these findings is presented in the next two sections.

Weak Solutions to the Euler Equations

To understand the way in which the discretized form of the Euler equations models a vortex sheet, it is first necessary to understand the way in which the partial differential equations themselves model a vortex sheet. The vortex sheet is a weak solution to the Euler equations.[18] If the Euler equations are written in the form

$$\frac{\partial}{\partial t}\boldsymbol{U}+\frac{\partial}{\partial x}\boldsymbol{F}(\boldsymbol{U})+\frac{\partial}{\partial y}\boldsymbol{G}(\boldsymbol{U})+\frac{\partial}{\partial z}\boldsymbol{H}(\boldsymbol{U})=0 \quad (15)$$

then a weak solution $\boldsymbol{U}$ is defined by

$$\int\int\int\int\left[\frac{\partial}{\partial t}\boldsymbol{T}\cdot\boldsymbol{U}+\frac{\partial}{\partial x}\boldsymbol{T}\cdot\boldsymbol{F}+\frac{\partial}{\partial y}\boldsymbol{T}\cdot\boldsymbol{G}+\frac{\partial}{\partial z}\boldsymbol{T}\cdot\boldsymbol{H}\right]\mathrm{d}x\,\mathrm{d}y\,\mathrm{d}z\,\mathrm{d}t=0 \quad (16)$$

for any vector test function $\boldsymbol{T}$ that is infinitely differentiable and vanishes at infinity. Carrying out the integration gives

$$U_s[\boldsymbol{U}]+\boldsymbol{n}_x[\boldsymbol{F}]+\boldsymbol{n}_y[\boldsymbol{G}]+\boldsymbol{n}_z[\boldsymbol{H}]=0 \quad (17)$$

in which $\boldsymbol{n}$ is a vector perpendicular to the surface of discontinuity, $\boldsymbol{U}_s$ is the velocity at which the surface is moving, and the square brackets denote the jump in a quantity across the surface. It should be noted that these relations are invariant to the conical self-similarity approximation, which simply states that the radial component of $\boldsymbol{n}$ is zero. The equations may be rewritten in the form

$$\text{Continuity:}\quad \rho_L[\boldsymbol{n}\cdot\boldsymbol{u}_L-U_s]=\rho_R[\boldsymbol{n}\cdot\boldsymbol{u}_R-U_s]=M$$

$$\text{Momentum:}\quad M[\boldsymbol{u}_R-\boldsymbol{u}_L]=\boldsymbol{n}[p_L-p_R]$$

$$\text{Energy:}\quad M\left[h_{0_R}-h_{0_L}\right]=0 \quad (18)$$

in which the subscripts L and R denote the left and right sides of the sheet, respectively. The momentum equations may be rewritten in a more convenient form by resolving them into normal and tangential coordinates. They become

$$M[\boldsymbol{n}\cdot\boldsymbol{u}_R-\boldsymbol{n}\cdot\boldsymbol{u}_L]=p_L-p_R$$

$$M[\boldsymbol{n}\times\boldsymbol{u}_R-\boldsymbol{n}\times\boldsymbol{u}_L]=0 \quad (19)$$

It is now clear that there are two possible types of discontinuous solutions:

1) $\boldsymbol{n}\times\boldsymbol{u}$ is continuous across the sheet. The relations are

$$\rho_L\left[u_{n_L}-U_s\right]=\rho_R\left[u_{n_R}-U_s\right]=M$$

$$M\left[u_{n_R}-u_{n_L}\right]=p_L-p_R$$

$$h_{0_R}-h_{0_L}=0$$

$$u_{t_R}-u_{t_L}=0 \quad (20)$$

plus the equation of state and the definition of total enthalpy. This yields seven equations in seven unknowns describing a discontinuity in normal velocity.

2) $M=0$. The relations are

$$u_{n_R}=u_{n_L}=U_s$$

$$p_R=p_L \quad (21)$$

plus the equation of state and definition of total enthalpy. This yields four equations in seven unknowns, describing a contact discontinuity.

In the following, only the tangential velocity discontinuity will be considered. It will be assumed that the boundary conditions enforce that the jumps in density and total enthalpy across the sheet are zero.

Model for the Total Pressure Loss

The primary characteristic of the contact discontinuity weak solution is that the energy equation and the tangential momentum equations are degenerate, due to the zero mass-flux condition. For the discretized Euler equations to support a solution with the proper jump conditions, they must show the same level of degeneracy as the partial differential equations. To see this, the discretized Euler equations are cast in a form analogous to equation set 18. In the following, a Cartesian grid will be considered for the sake of simplicity. Carrying out the flux balance for the finite volume scheme, the discretized

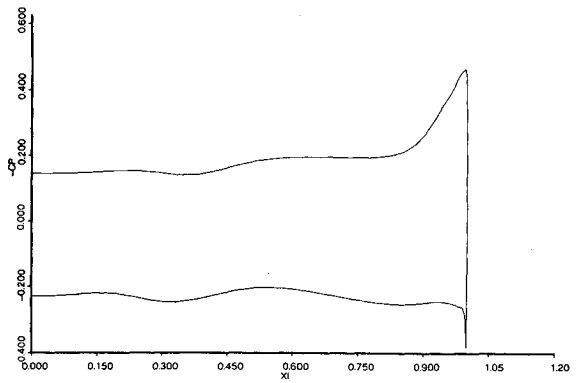

a) Pressure coefficient at 50 iterations.

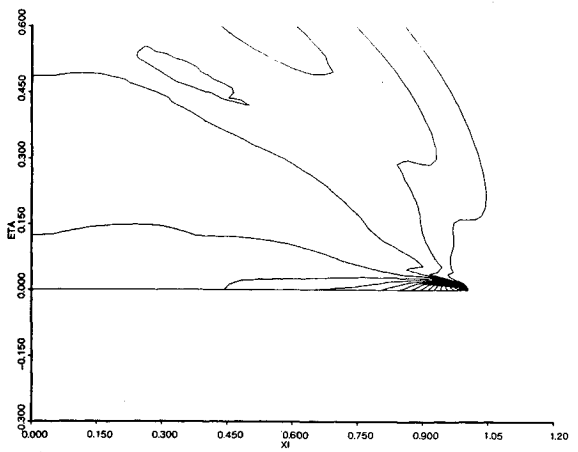

b) Total pressure loss at 50 iterations (increment = 0.04).

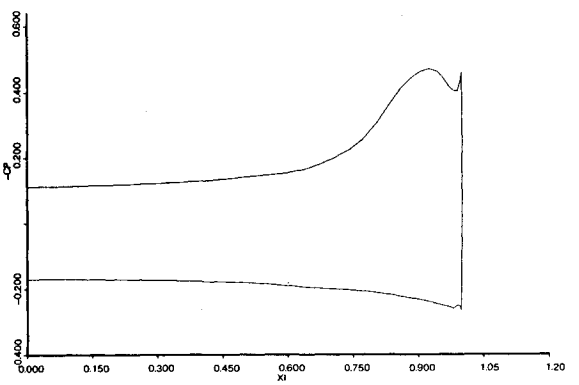

c) Pressure coefficient at 100 iterations.

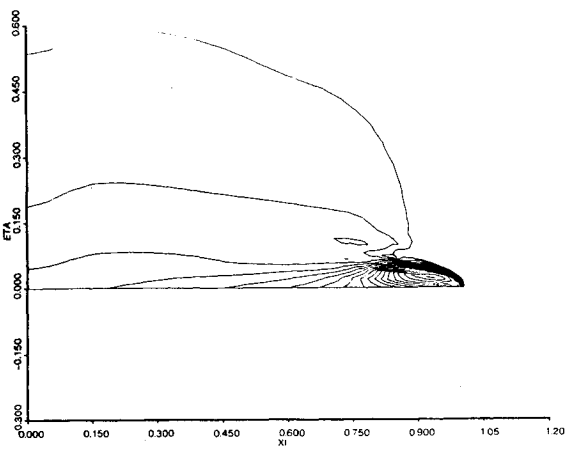

d) Total pressure loss at 100 iterations (increment = 0.04).

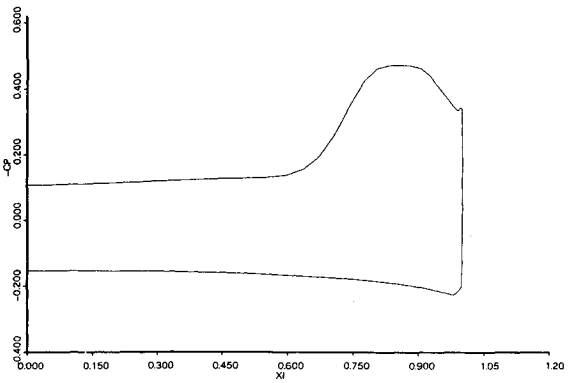

e) Pressure coefficient at 150 iterations.

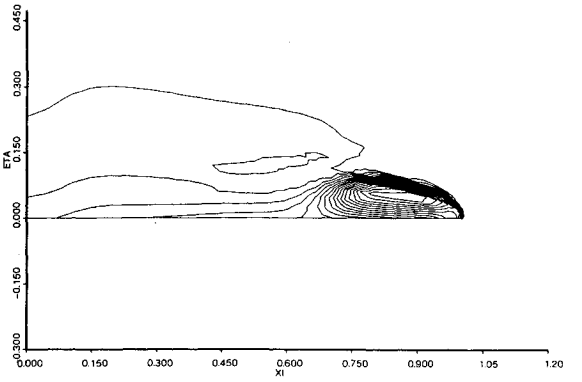

f) Total pressure loss at 150 iterations (increment = 0.04).

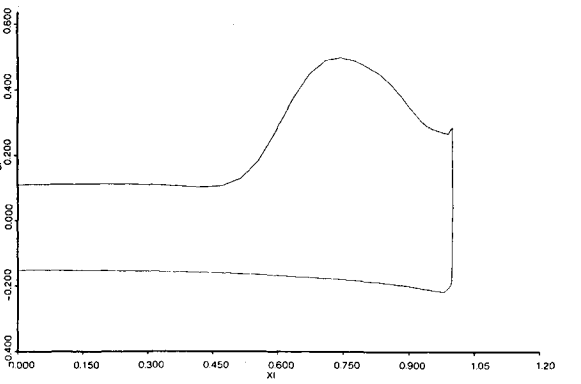

g) Pressure coefficient at 300 iterations.

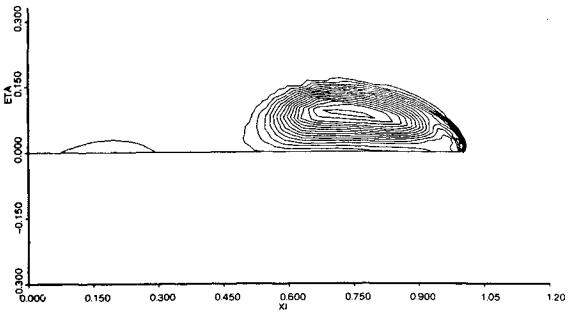

h) Total pressure loss at 300 iterations (increment = 0.04).

Fig. 7 Vortex evolution.

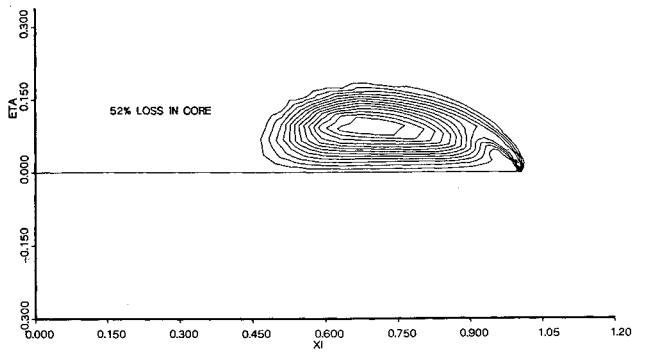

a) $\nu_2 = 0.01$, $\nu_4 = 0.01$ (increment = 0.04).

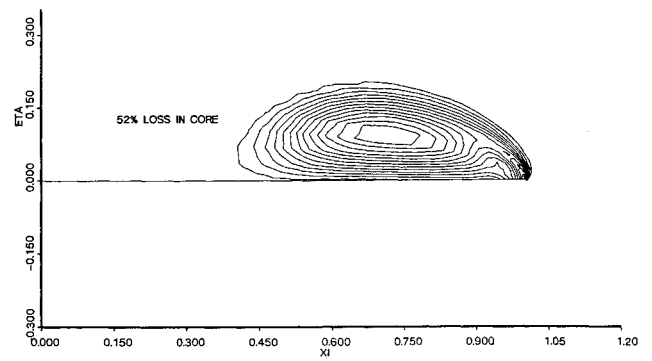

b) $\nu_2 = 0.10$, $\nu_4 = 0.01$ (increment = 0.04).

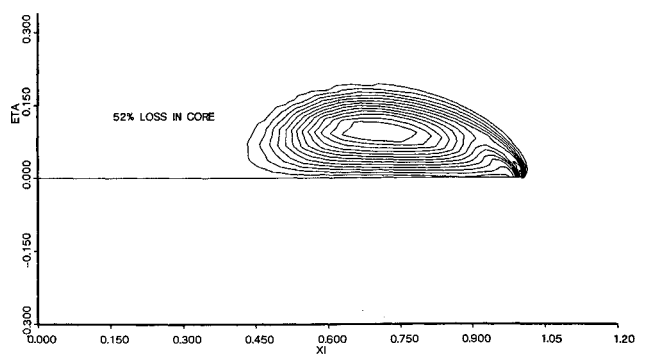

c) $\nu_2 = 0.05$, $\nu_4 = 0.02$ (increment = 0.04).

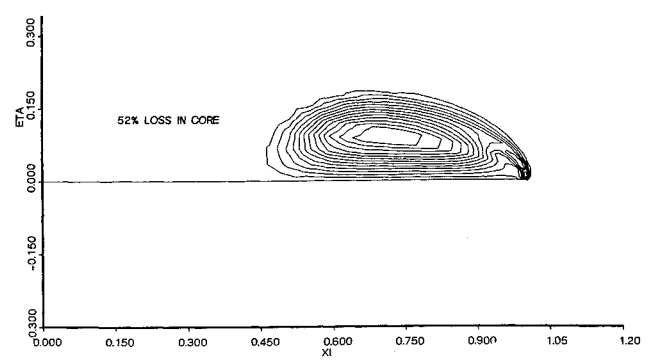

d) $\nu_2 = 0.05$, $\nu_4 = 0.002$ (increment = 0.04).

Fig. 8 Total pressure loss contours.

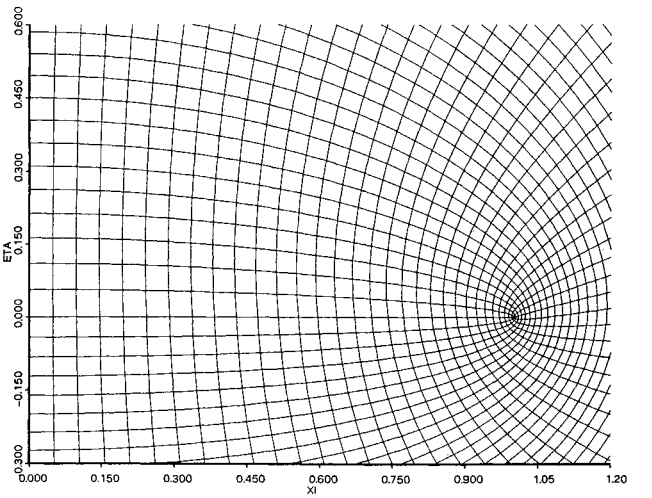

a) Grid, $\beta = 1.5$.

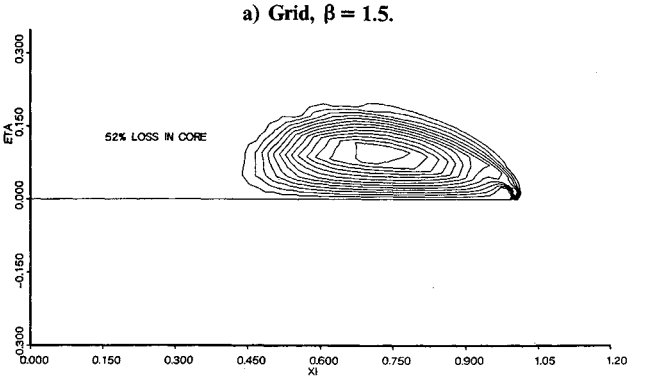

b) Total pressure loss contours, $\beta = 1.5$ (increment = 0.04).

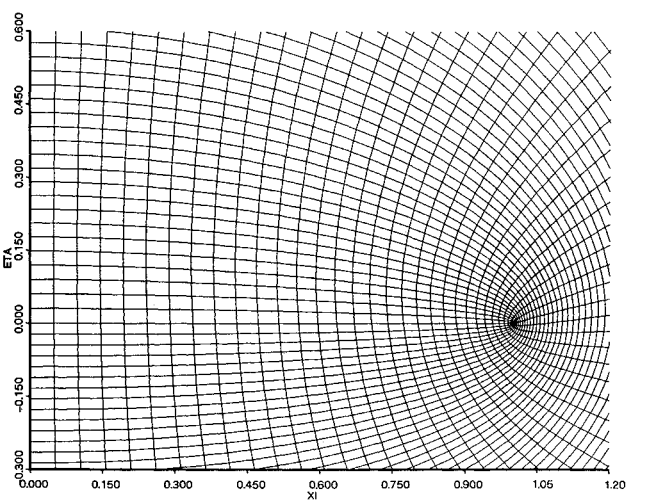

c) Grid, $\beta = 3.5$.

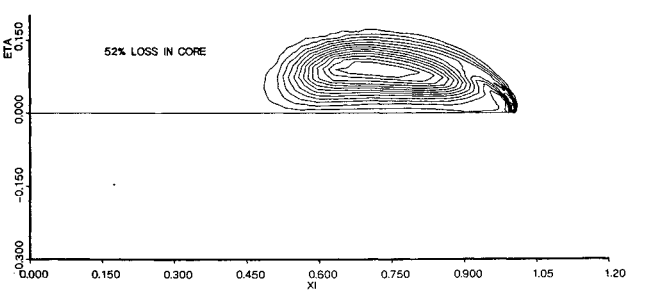

d) Total pressure loss contours, $\beta = 3.5$ (increment = 0.04).

Fig. 9 Effect of change in grid distribution.

Euler equations become

$$A\frac{\partial}{\partial t}\begin{bmatrix}\rho\\ \rho u\\ \rho v\\ \rho w\\ \rho E\end{bmatrix}+\begin{bmatrix}1 & 1 & 1 & 1 & 1 & 1\\ u_{x+} & u_{x-} & u_{y+} & u_{y-} & u_{z+} & u_{z-}\\ v_{x+} & v_{x-} & v_{y+} & v_{y-} & v_{z+} & v_{z-}\\ w_{x+} & w_{x-} & w_{y+} & w_{y-} & w_{z+} & w_{z-}\\ h_{0_{x+}} & h_{0_{x-}} & h_{0_{y+}} & h_{0_{y-}} & h_{0_{z+}} & h_{0_{z-}}\end{bmatrix}\times\begin{bmatrix}M_{x+}\\ M_{x-}\\ M_{y+}\\ M_{y-}\\ M_{z+}\\ M_{z-}\end{bmatrix}+\begin{bmatrix}0\\ P_{x+}-P_{x-}\\ P_{y+}-P_{y-}\\ P_{z+}-P_{z-}\\ 0\end{bmatrix}=0 \tag{22}$$

in which the subscripts denote cell faces with positive or negative normals, M denotes the mass flux through a face and P denotes the pressure force on a face. This form of the discrete equations is analogous to equation set 18. The temporal terms of this discretized equation set replace the U_s term in the definition of M.

For the purpose of illustration, a simple case is considered here. The energy equation is replaced by a constant total enthalpy condition§ and the flow is assumed to be quasi-one-dimensional, i.e., all y and z derivatives are assumed to be zero, and the z-direction momentum equation is dropped. Equation 22 becomes

$$A\frac{\partial}{\partial t}\begin{bmatrix}\rho\\ \rho u\\ \rho v\end{bmatrix}+\begin{bmatrix}1 & 1\\ u_{x+} & u_{x-}\\ v_{x+} & v_{x-}\end{bmatrix}\begin{bmatrix}M_{x+}\\ M_{x-}\end{bmatrix}+\begin{bmatrix}0\\ P_{x+}-P_{x-}\\ 0\end{bmatrix}=0 \tag{23}$$

In the simple case in which $u=0$ throughout the field, these equations and the constant total enthalpy relation become

$$\text{Continuity:}\quad \frac{\partial\rho}{\partial t}=0$$

$$x\text{ momentum:}\quad A\frac{\partial}{\partial t}(\rho u)+(P_{x+}-P_{x-})=0$$

$$y\text{ momentum:}\quad \frac{\partial}{\partial t}(\rho v)=0$$

$$\text{Energy:}\quad -\Delta v^2=\frac{2\gamma}{\gamma-1}\Delta\left(\frac{p}{\rho}\right) \tag{24}$$

If a jump in v occurs between two points such that v^2 is constant everywhere, there is no mechanism to change the pressure and, therefore, no mechanism to change any of the variables. This implies that the discrete equations permit a steady, quasi-one-dimensional, constant-presure vortex sheet *if it is a two-point sheet*. If the jump in v is spread over more than two points, there will be a deficit in v^2 inside the sheet. The constant total enthalpy condition implies that any deficit in v^2, $-\Delta v^2$, must be balanced by a change in p/ρ. Thus, a sheet spread across more than two points will have nonconstant properties within the structure of the sheet.

In the case of $u\neq 0$, the equation set is no longer degenerate, since M_{x+} and M_{x-} are nonzero. The y momentum equation will have a nonzero contribution from the flux balance. The integration in time will, therefore, cause the jump in v to spread across more than two points, leading to a deficit in v^2 inside the sheet. This deficit in v^2 will be balanced by changes in u^2 and p/ρ such that

$$-\Delta v^2=\frac{2\gamma}{\gamma-1}\Delta\left(\frac{p}{\rho}\right)+\Delta(u^2) \tag{25}$$

This will yield a corresponding loss in total pressure.

The remaining figures present results for a quasi-one-dimensional model problem, with the energy equation included. The initial conditions for the problem are

$$\begin{aligned}u&=u_\infty\\ v&=v_\infty \quad i<i_{\max}/2\\ &=-v_\infty \quad i\geq i_{\max}/2\\ p&=p_\infty\\ \rho&=\rho_\infty\end{aligned} \tag{26}$$

The quantities plotted are

$$\frac{v}{v_\infty}-1\qquad \frac{u}{u_\infty}-1\qquad \frac{p}{p_\infty}-1$$

$$\frac{p_t}{p_{t\infty}}-1\qquad \frac{h_0}{h_{0\infty}}-1\qquad \frac{\rho}{\rho_\infty}-1 \tag{27}$$

Figures 11a and 11b show the results for $U_\infty=0$ after several iterations. In the case of zero damping, the two-point sheet remains steady. Any added damping causes the sheet to spread. The pressure remains constant within the sheet. There is a decrease in the density to balance the deficit in v^2. Figures 11c and 11d are the results for $U_\infty\neq 0$ after several iterations, when the sheet is spread over four points. The density remains constant within the sheet. The pressure rise is seen to very with Δv^2, as expected. The total enthalpy varies through the sheet, due to the nonzero unsteady energy term.

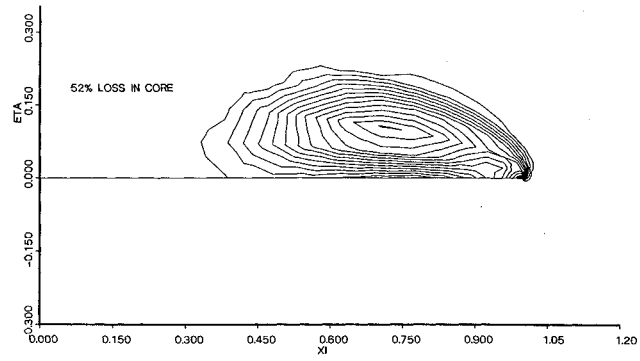

a) $i_{\max}=j_{\max}=32$ (increment = 0.04).

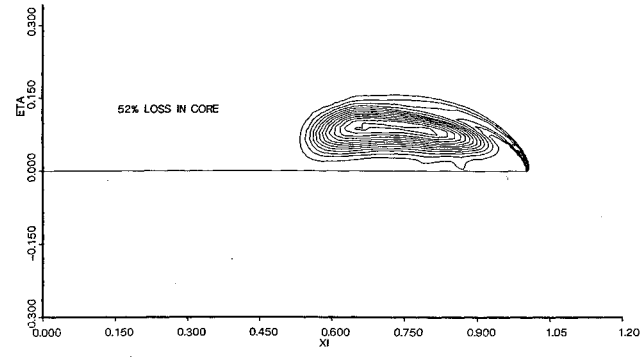

b) $i_{\max}=j_{\max}=128$ (increment = 0.04).

Fig. 10 Total pressure loss contours.

§For the results in this paper, h_0 is constant to less than 0.1%.

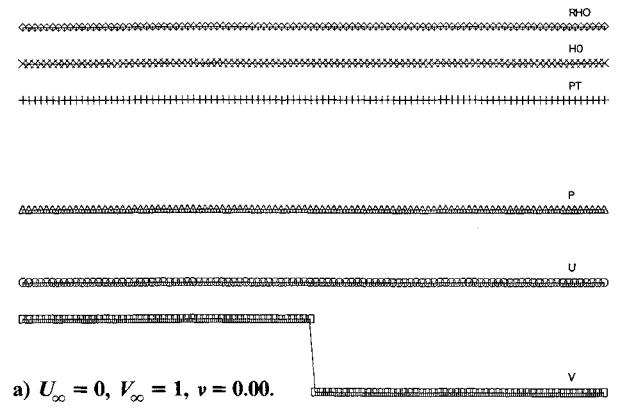

a) $U_\infty = 0$, $V_\infty = 1$, $v = 0.00$.

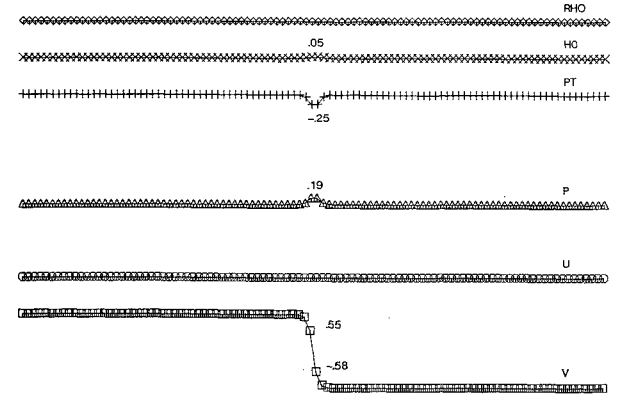

b) $U_\infty = 0$, $V_\infty = 1$, $v = 0.05$.

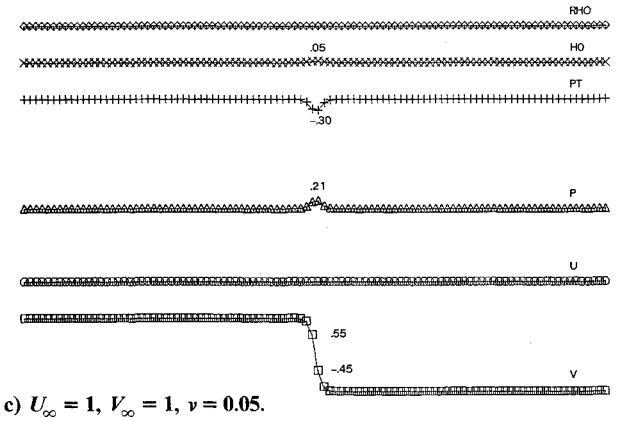

c) $U_\infty = 1$, $V_\infty = 1$, $v = 0.05$.

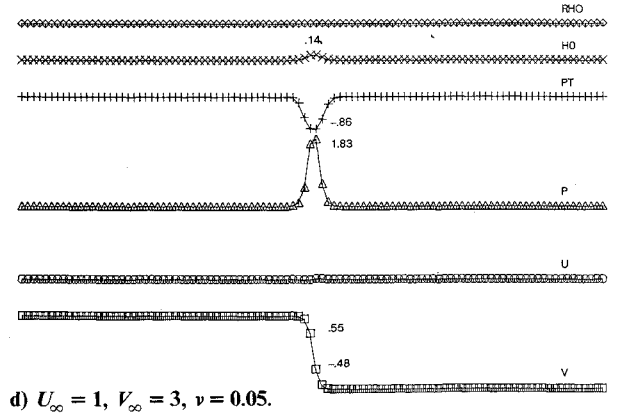

d) $U_\infty = 1$, $V_\infty = 3$, $v = 0.05$.

Fig. 11 Model problem results.

It is important to note that the base level of the pressure rise and the total pressure loss are set not by the way that the sheet is discretized, but the fact that the sheet is discretized at all. They are a function of the strength of the sheet, rather than the thickness of the sheet. Computational parameters, such as the grid spacing and the added artificial viscosity, do affect the loss, but only to higher order. The base level of the total pressure loss is set by the ratio of the square of the tangential velocity to the square of the total velocity, via the constant total enthalpy condition. This holds for the two-dimensional and three-dimensional cases as well.

The results for the delta wing are seen to be consistent with this model. The vortex is modeled as a viscous-like core, rather than a spiralling vortex sheet. The cross-flow Mach number (Fig. 4) goes to zero at the core of the vortex. The total pressure loss of 52% in the core is consistent with the relation of cross-flow Mach number to radial Mach number (Fig. 5) outside the vortex. Computational parameters have very little effect on the level of this loss.

Conclusions

There is a fundamental difference between the contact discontinuity weak solution to the Euler equations and the analogous solution to the discretized Euler equations. The jump conditions for the Euler equations are degenerate, due to the zero mass flux across the sheet. The discretized equations are not degenerate in this way and, therefore, do not enforce constant properties through the sheet. Instead, there is a change in the pressure, density and normal velocity inside the sheet, to balance the deficit in tangential velocity such that constant total enthalpy is maintained. This results in a loss in total pressure. The level of this total pressure loss is set by the ratio of the square of the tangential velocity (the cross-flow velocity in the delta-wing examples presented here) and the square of the total velocity. Varying the grid resolution or artificial viscosity by an order of magnitude changes the magnitude of the total pressure loss by less than 2%.

It is clear, then, that vortex sheet capturing, regardless of the mesh refinement, will give a solution with a total pressure loss inside the vortex. This total pressure loss is brought about by the fact that the discretization of the vortex sheet gives it a finite thickness. Despite the fact that the captured "sheet" has a finite thickness and structure, the conditions on either side of the "sheet" will agree with the weak solution of the Euler equations for suitably refined grids. The actual physical problem will have a total pressure loss at least as large as that predicted by the discretized Euler equations. There will be an added momentum deficit due to the boundary layer from the wing, in addition to the deficit in the tangential velocity.

References

[1] Miller, D.S. and Wood, R.M., "An Investigation of Wing Leading-Edge Vortices at Supersonic Speeds," AIAA Paper 83-1816, July 1983.

[2] Johnson, F.T., Tinoco, E.N., Lu, P., and Epton, M.A., "Three-Dimensional Flow over Wings with Leading-Edge Vortex Separation," *AIAA Journal*, Vol. 18, April 1980, pp. 367–380.

[3] Rizzi, A., Eriksson, L.E., Schmidt, W., and Hitzel, S., "Numerical Solutions of the Euler Equations Simulating Vortex Flows around Wings," *Aerodynamics of Vortical Type Flows in Three Dimensions*, AGARD-CP-342, April 1983, Paper 21.

[4] Weiland, C., "Vortex Flow Simulations past Wings Using the Euler Equations," *Aerodynamics of Vortical Type Flows in Three Dimensions*, AGARD-CP-342, April 1983, Paper 19.

[5] Raj, P. and Sikora, J.S., "Free-Vortex Flows: Recent Encounters with an Euler Code," AIAA Paper 84-0135, Jan. 1984.

[6] Rizetta, D.P. and Shang, J.S., "Numerical Simulation of Leading-Edge Vortex Flows," AIAA Paper 84-1544, June 1984.

[7] Fujii, K. and Kutler, P., "Numerical Simulation of the Viscous Flow Fields over Three-Dimensional Complicated Geometries," AIAA Paper 84-1550, June 1984.

[8]Newsome, R.W., "A Comparison of Euler and Navier-Stokes Solutions for Supersonic Flow over a Conical Delta Wing," AIAA Paper 85-0111, Jan. 1985.

[9]Hoeijmakers, H.W.M., "Computational Vortex Flow Aerodynamics," *Aerodynamics of Vortical Type Flows in Three Dimensions*, AGARD-CP-342, April 1983, Paper 18.

[10]Rizzi, A., "Euler Solutions of Transonic Vortex Flow around the Dillner Wing—Compared and Analyzed," AIAA Paper 84-2142, Aug. 1984.

[11]Jameson, A., Leicher, S., and Dawson, J., "Remarks on the Development of a Multiblock Three-Dimensional Euler Code for Out-of-Core and Multiprocessor Calculations," *Progress and Supercomputing in Computational Fluid Dynamics*, Birkhauser, Boston, 1985, pp. 53–66.

[12]Murman, E., Rizzi, A., and Powell, K., "High Resolution Solutions of the Euler Equations for Vortex Flows," *Progress and Supercomputing in Computational Fluid Dynamics*, Birkhauser, Boston, 1985, pp. 93–113.

[13]Perez, E., "Computation of Conical Flows with Leading-Edge Vortices," Master's Thesis, Massachusetts Institute of Technology, Cambridge, Aug. 1984.

[14]Powell, K., "The Effects of Artificial Viscosity Models on Conically Self-Similar Solutions to the Euler Equations," Master's Thesis, Massachusetts Institute of Technology, Cambridge, Aug. 1984.

[15]Jameson, A., Schmidt, W., and Turkel, E., "Numerical Solutions of the Euler Equations by a Finite Volume Method Using Runge-Kutta Time-Stepping Schemes," AIAA Paper 81-1259, June 1981.

[16]Rizzi, A. and Eriksson, L.E., "Computation of Flow around Wings Based on the Euler Equations," *Journal of Fluid Mechanics*, Vol. 148, Nov. 1984.

[17]Marconi, F., "The Spiral Singularity in the Supersonic Inviscid Flow over a Cone," AIAA Paper 83-1665, July 1983.

[18]Richtmyer, R.D., *Principles of Advanced Mathematical Physics*, Vol. 1, Springer-Verlag, New York, 1978.